Effects of grain size distribution and stress heterogeneity on yield stress of polycrystals: A numerical approach

Francis Lavergne, Renald Brenner, Karam Sab

▶ **To cite this version:**

Francis Lavergne, Renald Brenner, Karam Sab. Effects of grain size distribution and stress heterogeneity on yield stress of polycrystals: A numerical approach. Computational Materials Science, 2013, 77, pp.387-398. 10.1016/j.commatsci.2013.04.061 . hal-00946087

HAL Id: hal-00946087

https://enpc.hal.science/hal-00946087v1

Submitted on 29 Jan 2024

HAL is a multi-disciplinary open access archive for the deposit and dissemination of scientific research documents, whether they are published or not. The documents may come from teaching and research institutions in France or abroad, or from public or private research centers.

L'archive ouverte pluridisciplinaire **HAL**, est destinée au dépôt et à la diffusion de documents scientifiques de niveau recherche, publiés ou non, émanant des établissements d'enseignement et de recherche français ou étrangers, des laboratoires publics ou privés.

Effects of grain size distribution and stress heterogeneity on yield stress of polycrystals: A numerical approach

F. Lavergne[a], R. Brenner[b,*], K. Sab[a]

[a]Université Paris-Est, Laboratoire Navier (UMR 8205), CNRS, ENPC, IFSTTAR, F-77455 Marne-la-Vallée, France
[b]Institut Jean Le Rond d'Alembert, UMR 7190, Université Pierre et Marie Curie, CNRS, 75252 Paris Cedex 05, France

This paper addresses the relation between the grain size distribution, the elastic stress field fluctuations and the description of incipient plasticity in polycrystals with local elastic anisotropy. We propose a numerical approach based on full-field computations on polycrystalline microstructures. The generation of microstructures with prescribed grain size distribution and grain shape is made by combining dense-sphere packing with Power diagrams. By using a local plastic criterion based on the stress field statistics, it is shown that the macroscopic Hall–Petch relation significantly depends on the grain size distribution and the stress heterogeneity. Previous results of the literature obtained with mean-field approaches are confirmed by our study.

1. Introduction

A polycrystalline material is a heterogeneous material with a random microstructure whose heterogeneity originates from the spatial variation of the crystalline orientation field together with the anisotropy of the single crystal. When the characteristic size of the grains is of the order of hundreds of μm or more, the statistical information on the morphological and crystallographic textures, based on *n*-point correlation functions, allows to derive bounds and estimates for effective linear (elasticity, conductivity, etc.) and nonlinear (plastic yield stress, electric hysteresis, etc.) properties [1,2]. These estimates depend on the shape of the correlation functions but not on their characteristic lengths. However, for polycrystals with smaller grain size, the effective properties may exhibit a dependence with the characteristic size of the heterogeneities. Consequently, the sole information on the shape of the *n*th order probability density functions is inadequate. In plasticity, a well-known relation exists between the grain size and the yield stress: the Hall–Petch effect [3,4]. It predicts a linear increase of the yield stress with respect to the inverse of the square root of the grain size. The modeling of this dependence can be addressed by using strain gradient plasticity models with higher order stresses [5–7] or by introducing geometrically necessary dislocations [8], whose density is related to the gradient of the plastic slip [9,10]. An alternative (phenomenological) approach is to consider a classical framework with a grain size dependence of parameters of the constitutive behavior (namely, the critical resolved shear stresses). This approach has been initially proposed in the context of the self-consistent scheme with a Hall–Petch type relation for the critical resolved shear stress on each slip system [11] for polycrystals with uniform grain size. The influence of a grain size distribution on the yield stress has been later investigated with the Taylor model [12] and the self-consistent scheme [13]. These models consider the average stress field within the grains to describe the initial yield stress. This assumption is known to deliver irrealistic self-consistent estimates, in the case of a uniform grain size, for cubic polycrystals exhibiting elastic anisotropy [14]. It has been recently shown that this shortcoming only arises if the intragranular stress heterogeneity is not accounted for in the criterion describing the inception of plasticity. The early plastic yielding, which occurs well below the conventional macroscopic yield stress can be indeed described by the self-consistent model which in turn coincides with reference full-field results on polycrystalline aggregates [15]. Following these results, the present study aims at investigating the effect of elastic anisotropy on the initial yield surface of polycrystals by considering their grain size distribution. For this goal, we adopt a numerical full-field approach allowing to perform computations on 3D polycrystalline unit-cells with prescribed morphological parameters. More specifically, the Fast-Fourier Transform (FFT) method [16,17] is used since it permits efficient calculations (for periodic boundary-value problems) based on digital images of the microstructure. This feature is particularly attractive in the case of complex microstructures presenting a large number of grains with varying sizes.

The experimental characterization of three-dimensional polycrystalline microstructures has been recently made possible with the development of X-ray diffraction contrast tomography [18].

* Corresponding author. Tel.: +33 1 44 27 87 06.
E-mail address: renald.brenner@upmc.fr (R. Brenner).

Consequently, the description of the effective response and local fields of real polycrystalline samples is now conceivable [19,20]. However, such experimental data remain relatively scarce. An alternative procedure consists in reconstructing three-dimensional microstructures from EBSD orientation maps obtained by consecutive polishing. Albeit possible (see, for instance, [21]), this procedure is particularly tedious and implies the destruction of the investigated sample. Following these remarks, it appears that a workable full-field analysis on polycrystalline microstructures with various grain size distributions must rely in practice on artificial microstructures which match given morphological characteristics. Besides, this approach is relevant in view of the design of microstructures.

The paper is organized as follows. Firstly, we present the numerical scheme used for the generation of polycrystalline microstructures. It combines a dense-sphere packing algorithm [22] with Power diagrams [23]. Illustrative examples encompass unimodal, bimodal as well as lognormal grain size distributions. The ability of the method to build polycrystalline aggregates with anisotropic grain shape is also emphasized. Secondly, the initial yield surface of copper polycrystals with varying grain size distribution is studied based on a statistical description of the stress field. Previous mean-field results concerning the effective Hall–Petch relation [3,4] are confirmed and the importance of the intragranular stress heterogeneity is further highlighted.

2. Generation of microstructures

2.1. Coupling Laguerre diagrams with dense sphere packing: background

2.1.1. Voronoi and Laguerre diagrams

Voronoi diagrams are widely used to construct artificial polycrystalline microstructures since they mimic the homogeneous crystal growth process [24]. A Voronoi diagram (Fig. 1) is a partition of space D which relies on N initial points $g_i \in D$, $i \in [0,N]$ called *germs*. Each grain $G_i \subset D$ is defined as the subset containing all the points closer to one germ than any other germ. Let $p \in D$ a point in space D.

$$p \in G_i \Longleftrightarrow \forall j \neq i; \quad \|p - g_i\| < \|p - g_j\| \tag{1}$$

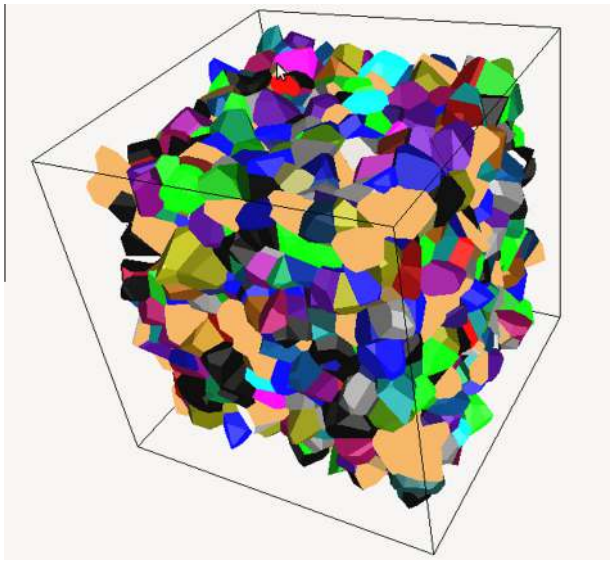

Fig. 1. A Poisson–Voronoi diagram with 2000 germs.

By construction, the interfaces between grains are planar and grains are convex polyhedra. Their faces can be obtained by using the Delaunay triangulation which is the dual graph of the Voronoi tessellation. Additional periodicity constraints have to be imposed on the tessellation to avoid artificial boundary effects.

The control of the grain volume distribution is obviously related to the spatial distribution of the germs. To represent equiaxed polycrystalline microstructures, a natural choice is to adopt a Poisson process to generate the germs. It leads to an isotropic microstructure with an almost uniform grain size. Dating from the work of Kumar et al. [25,26], this microstructural model is widely used to study the physical properties of equiaxed polycrystalline microstructures since it mimics the homogeneous crystal growth process[see, for instance, [27,28]]. By definition, this process provides no control on the microstructural features (i.e. grain size distribution and shape). To gain control on the grain repartition, a possibility is to adopt a Neyman-Scott or Gibbs process which helps obtaining aggregates of grains with different sizes [29]. However, the shape of the grains remains uncontrolled. An alternative approach to gain control on the grain size is to make use of Laguerre diagrams (also known as Power diagram) [23,30]. Each grain $G_i^L \subset D$ is now defined as the subset containing all the points for which the power distance relative to the sphere with center c_i and radius w_i is smaller than the power distance with any other spheres. The grain $G_i^L \subset D$ is defined as:

$$p \in G_i^L \Longleftrightarrow \forall j \neq i; \quad \|p - c_i\|^2 - w_i^2 < \|p - c_j\|^2 - w_j^2 \tag{2}$$

A Voronoi diagram is a Laguerre diagram for which all weights are equal. Interfaces between adjacent grains are planar and grains are convex polyhedra.

Laguerre diagrams and regular triangulations are dual. The vertices of the regular triangulation are the germs of the corresponding Power diagram, edges correspond to faces and the vertices of the Power diagram are the orthogonal centers of the triangulation [31]. Weight is similar to a distance and it enables some control of the size of grains. The larger the weight, the bigger the grain. If the germs c_i are randomly distributed, the Laguerre diagram can present the following shortcomings:

(i) The point c_i may not be within the grain G_i^L.
(ii) A germ may result in an empty grain.

Such problems are overcome when points c_i are taken as centers of non-overlapping spheres of radius $r_i \geqslant w_i$. In this particular case, each grain contains the sphere it comes from. If the volume fraction of the sphere packing is large enough, grains are expected to have low aspect ratios and the grain size distribution is expected to be similar to the diameter distribution of the spheres. Being able to pack efficiently dense sets of non-overlapping spheres can thus provide control on resulting grain size distribution and grain shape.

2.1.2. The Lubachevsky–Stillinger algorithm

To represent realistic polycrystalline microstructures, a Power diagram seeded by a random packing of spheres has been considered for this study. Many algorithms have been designed to study random dense packing of hard spheres. Among the most successful, the Lubachevsky–Stillinger (LS) algorithm [22] is able to fastly pack a large number of polydisperse spheres. It is possible to pack ellipsoids [32] and it has been used to generate random microstructures in the range of fiber-reinforced materials [33].

The LS algorithm is an event-driven molecular dynamic algorithm. At $t = 0$, spheres (Fig. 2) are reduced to points. Each radius increases proportionally to time t and each center moves with a constant velocity. As spheres collide, the algorithm changes their

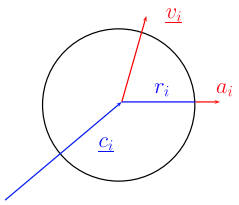

Fig. 2. A sphere in the Lubachevsky–Stillinger algorithm. Its center is $\underline{c_i}$ and its radius is r_i at time t_0. Its velocity is $\underline{v_i}$ and its growth rate is a_i.

velocities so as to avoid overlapping. The higher volume fraction for unimodal spheres is close to the densest possible.

Choosing constant rates of growth for the sphere radius and rectilinear uniform movements for centers enables analytic calculation of the time of collision between two spheres. Finding the next collision or the next time a sphere interacts with a planar boundary of the domain D is possible. As nothing happens until this event, the algorithm can jump to the time of this event without time stepping. The algorithm is therefore event-driven and this feature improves both speed and reliability.

Calculation of collision time is as follow: Let S_1,S_2 be two spheres of respective radius r_1, r_2 and center c_1, c_2 at time t_0. Let a_1, a_2 be their growth rate and v_1, v_2 their velocities. Collision occurs at time t if:

$$\|c_2 - c_1 + (t - t_0)(v_2 - v_1)\|^2 = (r_1 + r_2 + (a_1 + a_2)(t - t_0))^2$$

This quadratic equation has three cases:

1. It has no solution: the two spheres never collide.
2. It has one solution: the two spheres touch each other but do not overlap.
3. It has two solutions: the two spheres collide. Overlapping starts at first solution and ends at second solution.

Collisions are treated as described in [22]. The spheres bounce on each other almost elastically. Collisions are not elastic due to the growth of spheres which triggers a rise in the kinetic energy.

Cells of periodic microstructures are practical to perform homogenization studies. Combined with periodic boundary conditions, the elastic response does not exhibit bias related to boundary effet. Therefore, a periodic Power diagram was to be built and a periodic set of germ was needed. On the other hand, the periodic conditions on the microstructure must be taken in account while the spheres are growing: each time a sphere starts crossing a side of the periodic cell D, another sphere with same speed must enter on the opposite side. The two spheres must then have the same speed and growth ratio at every time. That is to say that if an event happens to the first one, the second one has to react in the same way. If a sphere gets out of D it can be deleted.

This method enables dense packing of spheres which will provide germs for a Laguerre diagram. The microstructure is expected to have almost spherical grains whose equivalent diameters follow a distribution similar to the one of the radius. It is worth noting that similar approaches have been previously proposed in different contexts [34–37].

2.2. Algorithmic details and improvements

2.2.1. Fast sphere packing

The Lubachevsky–Stillinger algorithm can be accelerated thanks to many algorithmic improvements [22]. These improvements [Algorithm 1] headed toward reducing the number of events to calculate and avoiding calculating them many times.

The cubic periodic cell is divided into many sectors. The domain is cut by planes and each subset created is a sector. The easiest way of doing so is to cut each dimension regularly so as to obtain cubes. A sphere must be added to a sector if whether some part of it may be in it. Therefore each time a sphere touches a boundary of a sector, it must be added to the sector on the other side. Those new event are created.

Two spheres that have no common sector cannot collide. As a result the number of events related to sphere-sphere collision is diminished. If there are N spheres in a cubic sector, $\frac{N(N-1)}{2}$ events of type sphere-sphere must be calculated and $6N$ events of type sphere-boundary. If we neglect the fact that a sphere can be in many sectors, it is advantageous to divide the periodic cubic cell since

$$\forall a > 0, b > 0, f(a+b) > f(a) + f(b) \quad \text{for} \quad f(x) = \frac{x(x-1)}{2} + 6x$$

By lowering the number of possible events, it is possible to stock their results with a reasonable memory usage.

Each sector keeps arraylists of the possible events and each event is given a flag indicating whether the event must be recalculated or not. At each iteration of the algorithm, events that are not up to date are calculated and the next event of each sector is found if needed. All the events are compared to determine the next event in the periodic cell. This event is executed and the events related to the changed spheres may be set as not up to date. It should be noted that the efficiency of this procedure decreases as the dispersion of grain size increases because big grains can collide with a large number of small ones.

Algorithm 1. Pack spheres

```
for All n_s spheres do
  Set rate of growth according to grain size distribution
  Pick random center and place in right sector
  Pick random velocity
end for
while time < time_of_max_volume_fraction do
  for All sectors do
    if sector is not up to date then
      for All possible event in the sector do
        Update the event, update next event in sector
      end for
    end if
    Get the next event in the sector
    if next event in sector earlier that current global next
  event then
      change current global next event
    end if
  end for
  if time of next global event < time_of_max_volume_fraction
   then
    Execute global next event (collision or sphere changing of
  sector)
    Declare involved spheres and sectors as not up to date:
  events need to be computed
  end if
  time = time of next global event
end while
time = time_of_max_volume_fraction
Compute positions and radius of all spheres at time
```

2.2.2. Discretization of microstructures

The use of the generated microstructures for FFT full-field computations [16] requires their discretization on a structured grid. As the grid may be large to obtain accurate results, the efficiency of this step is crucial. As linear search implies prohibitive computation times when the number of germs is large, an algorithmic

improvement has been used. As for the Lubachevsky–Stillinger algorithm, the space has been partitioned into sectors (Fig. 3). The search begins in the sector in witch the point p is. The closer germ is selected. The algorithm explores the sectors from the nearest to the further. It stops when unexplored sectors are further than the current selected germ. Therefore a smaller part of the periodic cell D is explored. Partitioning the cube D into cubic sectors makes it easier to find adjacent sectors and few tests are needed so as to check that further sectors are too far away. The periodicity of the microstructure is respected thanks to a modification of the distance calculation. Sectors of corresponding boundary of the microstructure must be connected. Some changes are done so as to discretize a Laguerre diagram. The weights of the germs have to be taken into account. The search remains the same except that the algorithm has to know how much the larger weight is so as to stop the search. The search stops when unexplored sectors are far enough. That is to say that if the heaviest germ was in those sectors, it could not be close enough to point p so as to have a lower power than current selected germ. This algorithmic improvement remains useful in case of various weights although the grain size

Table 1
Comparison of the dispersion parameter imposed on the growth rate of packed spheres and the one of the Laguerre–Voronoi cells

Sphere distribution	Expected σ	Observed σ	Number of grains used
Unimodal	0	0.02	5000
Lognormal $\sigma = 0.1$	0.10	0.082	5000
Lognormal $\sigma = 0.5$	0.5	0.35	20,000
Lognormal $\sigma = 1.0$	1.0	0.49	30,000

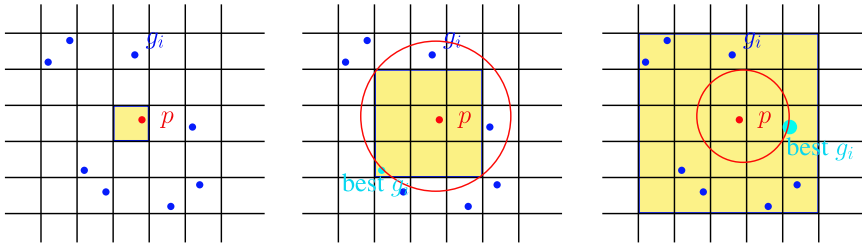

Fig. 3. Method for getting the nearest germ to point p. Further sectors are explored until finding a closer germ becomes impossible. This method is repeated for every voxel in the 3D image.

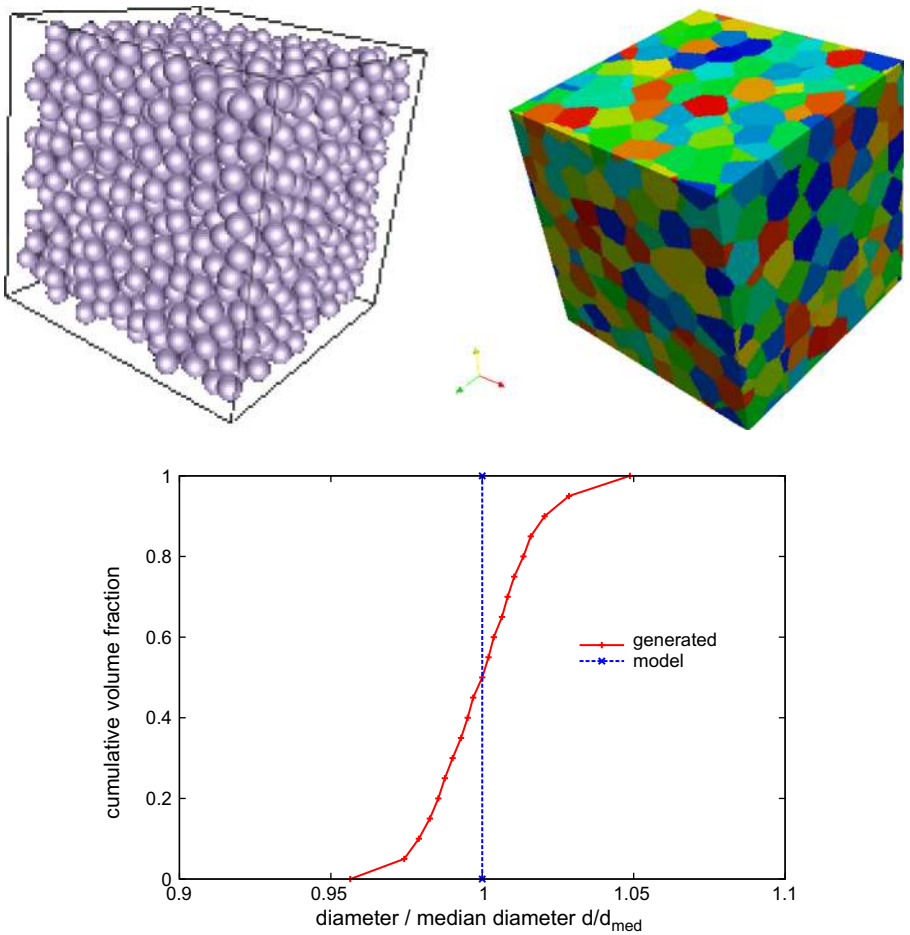

Fig. 4. Unimodal distribution: dense-sphere packing, Voronoi diagram corresponding to 500 spheres and comparison between the ideal and obtained grain size repartition function.

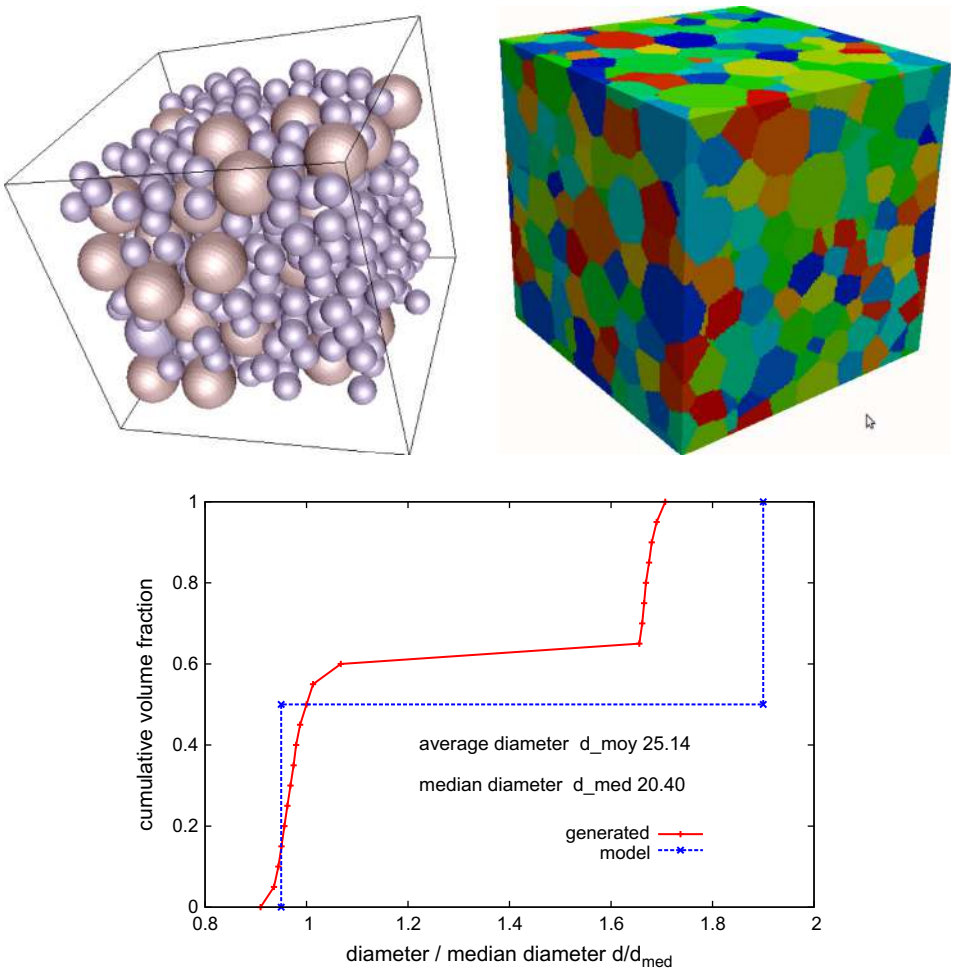

Fig. 5. Bimodal distribution: dense-sphere packing, Power diagram corresponding to 500 spheres and comparison between the ideal and obtained grain size repartition functions.

dispersion hinders the search for the germ the point belongs to. The algorithm has to explore sectors far away so as to discover whether the point p is in a big grain of not.

2.3. Results for various grain size distribution

2.3.1. Description of the generated microstructure

Various grain size distribution functions were investigated to assess the flexibility of the proposed method. Let n be the number of grains of the generated microstructure. Grain size distribution function has been estimated and statistical datas were calculated, namely:

- The average grain diameter: $D = \frac{1}{n}\sum_{i=1}^{n} D_i$.
- The standard deviation of grain diameter: $SD = \sqrt{\frac{1}{n}\sum_{i=1}^{n}(D_i - D)^2}$.

The dispersion parameter is defined as $\sigma = \sqrt{\log\left(\frac{SD^2}{D^2} - 1\right)}$. In the case of a lognormal grain size distribution, it represents the standard deviation of the variable $\log(D)$. For each kind of distribution, many (between 10 and 60 (Table 1)) sets of 500 grains have been generated to estimate the dispersion parameter.

2.3.2. Unimodal distribution

To produce an unimodal distribution function, we chose a uniform rate of growth for the spheres. Since all the seeds of the Power diagram have the same weight, the algorithm does produce a Poisson–Voronoi tessellation (Fig. 4). The volumic fraction of the sphere packing is set to 60% to avoid the appearance of regular sets of spheres. This volume fraction is similar to the parameter δ introduced in [24] to control the morphology of a Poisson–Voronoi tessellation.

2.3.3. Bimodal distribution

A bimodal microstructure has been considered with one value of grain diameter being twice the other. Ideally, each population of grains should fill half the volume of the cube. As shown in Fig. 5, the result is close to a bimodal microstructure with different parameters. The lower group of sizes represent 60% of the volume and the higher group is made of grains roughly 1.6 times larger in diameter instead of twice has big. These differences between the sphere's radius distribution and the grain size distribution can be attributed to the limit imposed on the total volume ratio (60%). The gap between the spheres has been captured by the smaller grains and the grain size dispersion is thus lower than the ideal (targeted) one.

2.3.4. Lognormal distribution

Lognormal distributions have been produced with various dispersion parameters: $\sigma = 0.1$, 0.5 or 1.0. A microstructure corresponding to $\sigma = 0.5$ is represented on Fig. 6. This distribution is imposed on the growth rate of the colliding spheres. The expected (ideal) and observed σ parameters have been compared (Table 1).

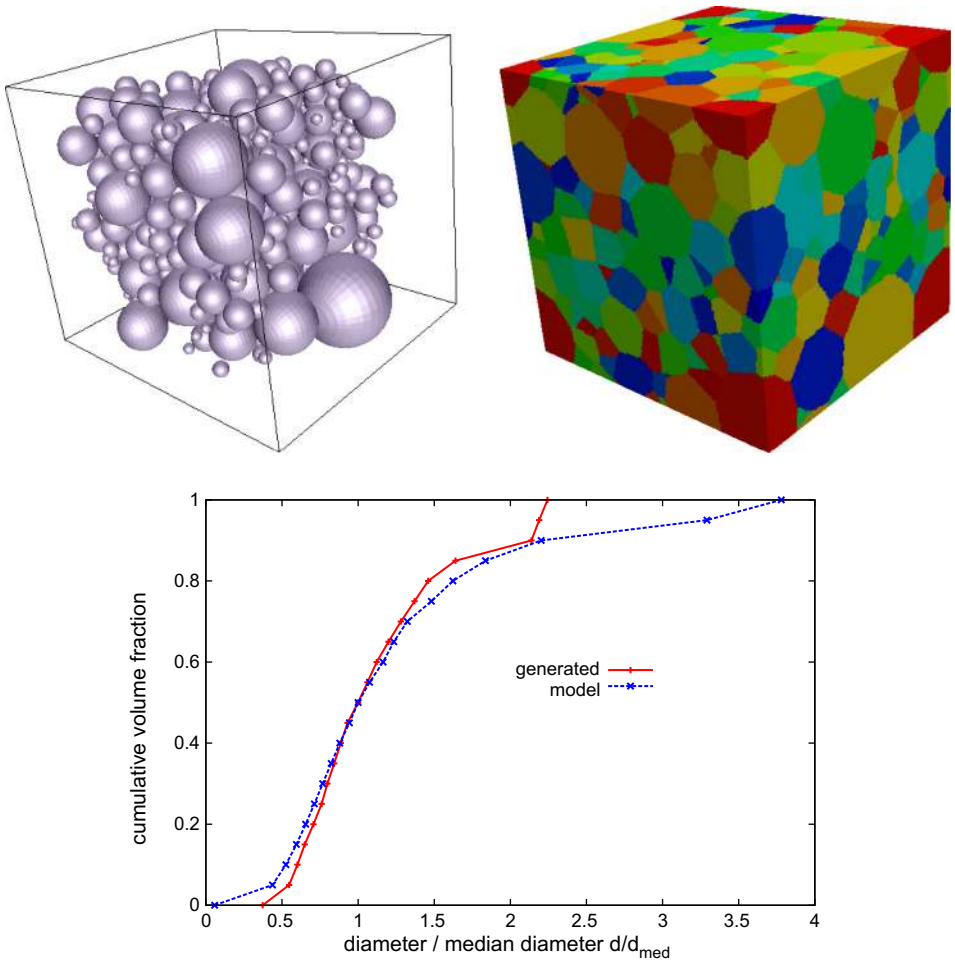

Fig. 6. Log-normal distribution: dense-sphere packing, Power diagram corresponding to 500 spheres and comparison between the ideal and obtained grain size repartition functions.

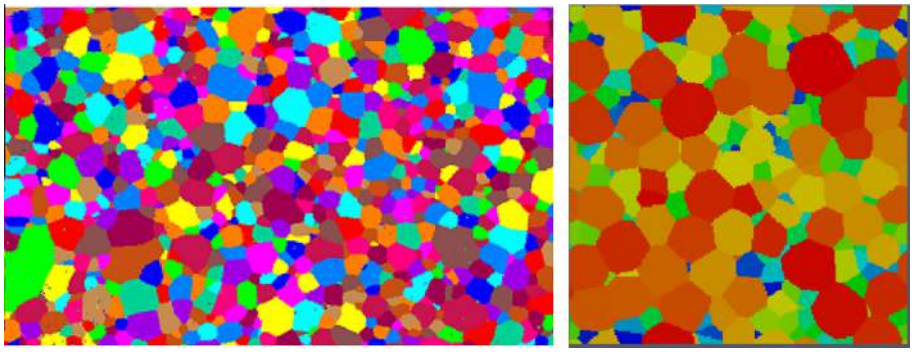

Fig. 7. Original EBSD map of a zirconium polycrystal (Left). Slice of the artificial microstructure built with experimental grain size distribution (Right).

The observed σ is lower than what was expected due to the fact that void between spheres has been captured by the smaller grains.

2.3.5. Experimentally measured distribution

When experimental data are available on the grain size distribution, it is obviously possible to build artificial microstructures matching this experimental information. As an illustration, a zirconium grain map obtained by electron-back scattered diffraction (EBSD) has been used as input for our microstructure builder. Based on the two-dimensional grain size distribution, the three-dimensional grain size repartition has been first determined by using standard stereological technics (Appendix A). Then, an artificial microstructure was generated based on this experimental information (Fig. 7).

2.4. Toward complex microstructures

The previous examples have shown the ability of the procedure to produce microstructures with equiaxed grains and prescribed diameter size distributions. This method has been extended to consider microstructures with anisotropic grains shape. Anisotropic microstructures with flat or thin grains are representative of

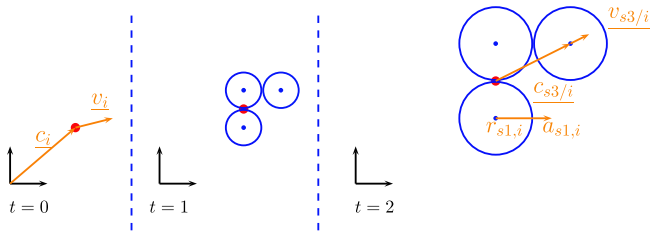

Fig. 8. Motion of a cluster of spheres. At time $t = 0$, the cluster is reduced to its center $\underline{c_i}$ and its velocity $\underline{v_i}$. As time goes by, the spheres are growing at their rates a_{sj} and they move away from the center of the cluster at velocity $\underline{v_{sj/i}}$.

laminated or extruded polycrystalline materials. Laguerre diagram are still used to keep planar interfaces but new grains are defined as union of former polyedra created by a set of germs close to one another. The grains remain connex if the position and weight of germs are appropriately chosen. The Lubachevsky–Stillinger algorithm has thus been modified to pack sets of spheres.

The modified procedure goes as follows: a cluster of spheres is reduced to its center C_n at starting time $t = 0$. Each sphere is defined at any time by its radius and its relative position to the center of the cluster. The center of the cluster is allowed to translate. At time $t > 0$, growing spheres are moving away from the center of the cluster along given directions so that the cluster is homothetic across time (Fig. 8). Rate of growth of spheres and branches are chosen constant and the center of the cluster has a constant velocity. These choices are motivated by the analytical computation of collision times.

The grain shape is expected to be close to the shape of the cluster of spheres if final volume ratio is high. Finally, it is worth mentioning that this packing method is particularly efficient in the case of elongated grains (Fig. 9) or flat grains with the same normal (Fig. 10).

3. Effect of grain size distribution on plastic inception

The microstructure builder has been used to address the question of the inception of plasticity in elastoplastic polycrystals whose grains are elastically anisotropic. This problem has been

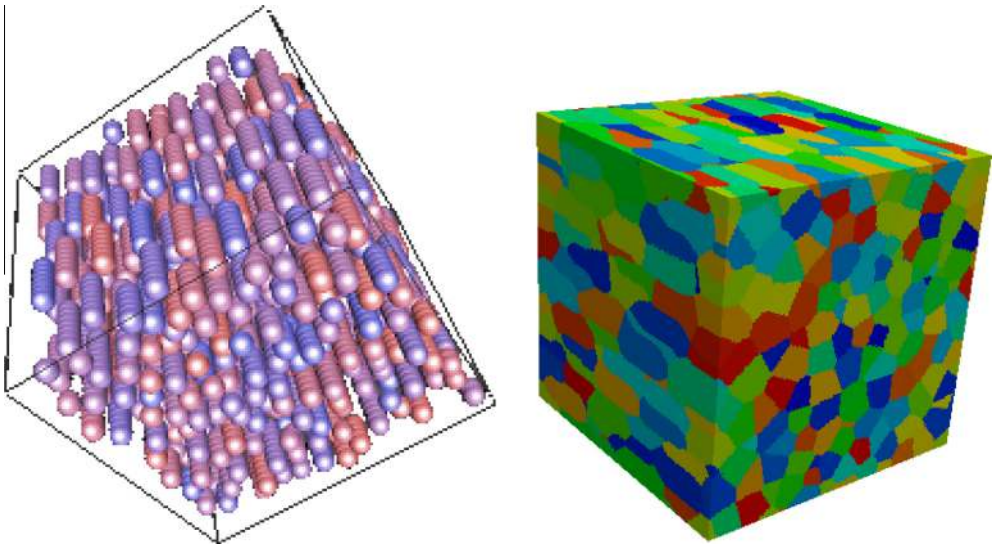

Fig. 9. Dense packing of sets of spheres and corresponding Laguerre diagram: case of elongated grains.

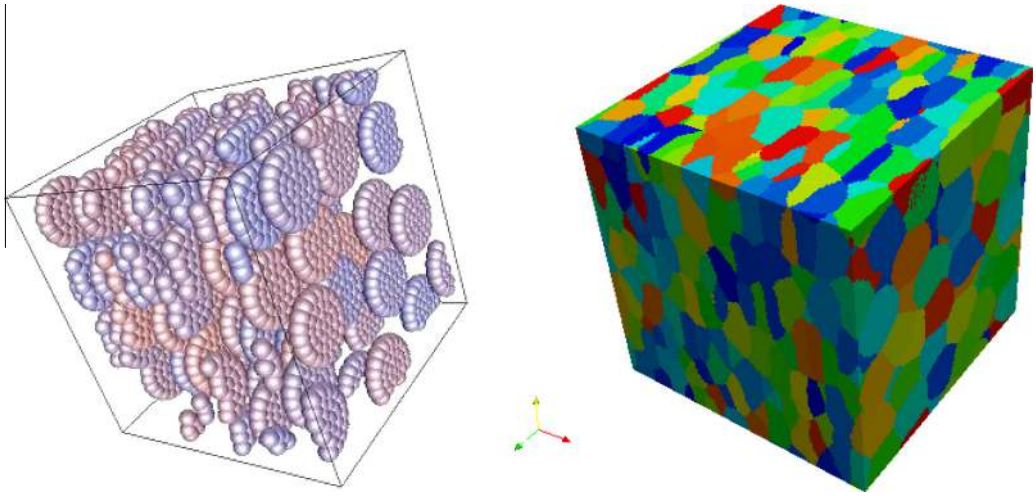

Fig. 10. Dense packing of sets of spheres and corresponding Laguerre diagram: case of flat grains.

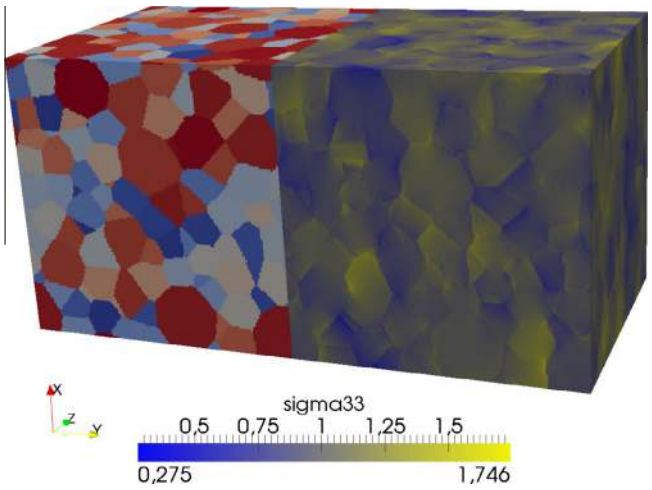

Fig. 11. Stress field fluctuations σ_{xx} in a polycrystal made of elastically anisotropic grains subjected to uniaxial tension along the **x** axis. The grid discretization is $144 \times 144 \times 144$.

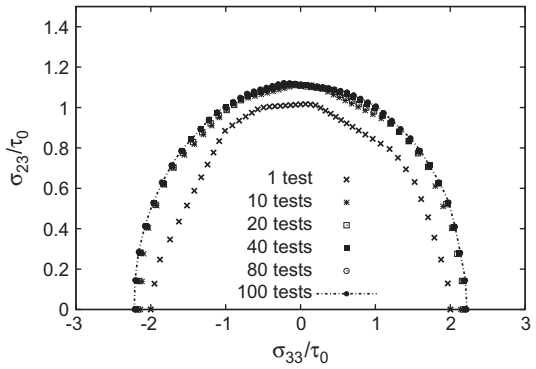

Fig. 12. Initial yield surface, for $p = 0$, averaged over different numbers of realizations. The parameter describing the yield criteria (volumic fraction of plastic grains) has been set to $\epsilon = 1\%$.

previously studied in [15] for polycrystals with an *uniform grain size*. In the sequel, it is extended to the case of polycrystals with a given grain size distribution. We adopt an explicit grain size dependence of the critical resolved shear stresses on each slip system and use is made of a yield criterion at the grain scale which depends on the intragranular stress field statistics.

3.1. Yield criterion incorporating stress field fluctuations

Let $\mathcal{N}_g$ the set of grains with different crystalline orientations and $\mathcal{K}$ the set of slip systems within each grain. The inception of plasticity within the polycrystal is defined by the following Schmid criterion.

$$\max_{r\in\mathcal{N}_g}\max_{k\in\mathcal{K}}\hat{\tau}_k^r = \tau_0^r \tag{3}$$

where the reference resolved shear stress $\hat{\tau}_k^r$ reads

$$\hat{\tau}_k^r = |\langle\tau_k\rangle_r| + p\ \mathrm{SD}^r(\tau_k) \quad \text{with} \quad p \in \mathbb{R}^+ \tag{4}$$

$\langle\tau_k\rangle_r$ is the intragranular average of the resolved shear stress on slip system k within grain r and $\mathrm{SD}_r(\tau_k)$ is its standard deviation

$$\mathrm{SD}^r(\tau_k) = \sqrt{\langle\tau_k^2\rangle - (\langle\tau_k\rangle_r)^2}. \tag{5}$$

These two quantities can be obtained by projection on the slip system k of the first and second moments of the intragranular stress field:

$$\langle\tau_k\rangle_r = \mu_k^r : \langle\boldsymbol{\sigma}\rangle_r \text{ and } \langle\tau_k^2\rangle_r = \mu_k^r : \langle\boldsymbol{\sigma}\otimes\boldsymbol{\sigma}\rangle_r : \mu_k^r \tag{6}$$

with μ_k^r the Schmid tensor of slip system k within grain r. In the present study, we have used a simple phenomenological Hall–Petch type relation at the slip system scale. The critical resolved shear stress within grain r is defined by

$$\tau_0^r = \tau_0 + \frac{k_0}{\sqrt{D_r}} \tag{7}$$

where D_r is the grain size (equivalent diameter).

3.2. Full-field computations

The FFT full-field numerical scheme is used to compute the distribution of the elastic stress field arising from the elastic anisotropy of the single crystal. The fluctuation of the stress field within the polycrystal is illustrated in Fig. 11. From this spatial distribution of the stress field, the first and second moments within each grain are computed to apply the proposed local yield criterion. Many microstructural realizations are considered to obtain ensemble averages and yield inception is defined as the stress loading such that a given volume fraction ($\epsilon = 1\%$) of all the grains reached the local criteria [Algorithm 2]. The convergence of the criteria and the effect of ϵ is studied in Figs. 12 and 13. The macroscopic yield criteria depends on the critical volume fraction of grain above the local criteria ϵ.

Algorithm 2. Computation of the initial yield surface

```
for i = 0;i < nb_required_microstructure;i ++do
  Build a new microstructure of nb_grain
  for All basic loadings do
    Compute the elastic response with FFT
  end for
  for All wanted loadings do
    Compute the elastic response as a linear combination of
   basic loadings
    for Every point p of the image do
      Update volume estimate of the grain r
      for Every slip system k of the grain r do
        Update ⟨τ_k⟩
        Update ⟨τ_k^2⟩
      end for
    end for
    for Every grain r do
      for Every slip system k of the grain r do
        Compute and store ⟨τ_k⟩_r
        Compute and store SD^r(τ_k)
      end for
    end for
  end for
end for
for All wanted loadings do
  for Every grain r do
    Compute and store the critical stress
  end for
end for
for All wanted loadings do
  Return the level of loading such that grains over their
   critical stress represent ϵ% of the total volume.
end for
```

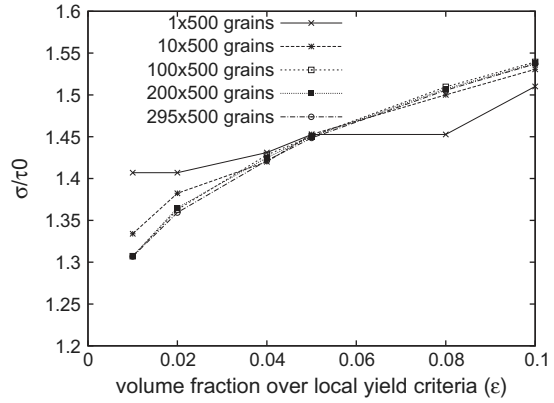

Fig. 13. Yield inception under uniaxial loading for $p = 0$ at different numbers of runs and for various ϵ. Here, the average diameter is 1 μm and the real dispersion is $\sigma = 0.34$.

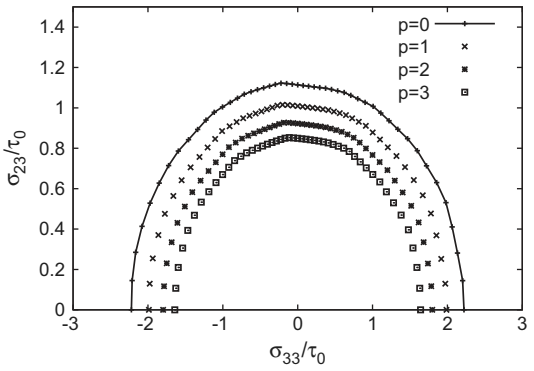

Fig. 14. Initial yield surface in tension–torsion according to the statistical yield criterion with different p values.

3.3. Self-consistent estimates

An alternative approach to estimate (partially) the statistical distribution of the local fields is to use the self-consistent model [40,41]. Indeed, in the framework of the mean-field estimates, the first and second moments of the stress field are given by

$$\langle \boldsymbol{\sigma} \rangle^r = (\mathbf{S}^r + \mathbf{S}^*)^{-1} : (\widetilde{\mathbf{S}} + \mathbf{S}^*) : \bar{\boldsymbol{\sigma}} \tag{8}$$

and

$$\langle \boldsymbol{\sigma} \otimes \boldsymbol{\sigma} \rangle^r_{ijkl} = \frac{1}{c_r} \bar{\boldsymbol{\sigma}} : \frac{\partial \widetilde{\mathbf{S}}}{\partial S^r_{ijkl}} : \bar{\boldsymbol{\sigma}} \tag{9}$$

$\langle \boldsymbol{\sigma} \rangle^r$ is the average stress in grain r and $\bar{\boldsymbol{\sigma}}$ is the macroscopic stress. $\mathbf{S}^r$ is the inverse of the stiffness tensor of grain r. $\widetilde{\mathbf{S}}$ is the effective compliance tensor and $\mathbf{S}^*$ is the inverse of the Hill constraint tensor. The reader is referred to [42,15] for further details on the computation of the statistics of the mechanical fields within polycrystals.

3.4. Results

3.4.1. Full-field computations for unimodal distribution

We have considered a single crystal elastic behavior similar to copper (Elastic coefficients: $C_{11} = 170$ GPa, $C_{12} = 124$ GPa and $C_{44} = 64$ GPa with Voigt notation). It corresponds to an anisotropy value (Zener parameter) of 2.8. Polycrystalline microstructures have been built with an unimodal grain size distribution and random crystalline orientation has been assigned to each grain. A detailed study on the influence of the discretization grid has been performed: the number of voxels per grain required to get an accurate estimate of the critical slip system (i.e. convergence of the first and second moments of the intragranular stress field) within the polycrystal has been determined (Table 2). Following this study, each microstructure made of 500 grains has been discretized on a grid of $144 \times 144 \times 144$ voxels. This corresponds to a resolution of 6000 voxels per grain.

The size of the elastic Representative Elementary Volume of copper was studied in 2005 in the frame defined by Kanit et al. [38]. Houdaigui et al. stated that 10 sets of 445 grains are required to compute its shear modulus with a precision of 1% [39].

The limit of the elastic domain have been computed for different modified Hutchinson criteria ($p = 0$, $p = 1$, $p = 2$ and $p = 3$) as proposed in [15]. Each microstructure comprises 500 grains and an unimodal grain size distribution was obtained with the microstructure builder. For each microstructure, two average elastic loadings were imposed and their responses were calculated. The problem being linear, it is straightforward to calculate the elastic response to any linear combination of these two loadings. The obtained yield surfaces are plotted in Fig. 14. As noted in [15], it is pointed out that the obtained ensemble average matches the estimate delivered by the self-consistent model for a given p value.

3.4.2. Effet of grain size dispersion and intragranular stress heterogeneity

To illustrate the additional effect of the grain size dispersion, we have considered log-normal grain size distributions with different

Table 3
Hall–Petch coefficients for $p = 0$ and various grain size dispersions.

Size distribution	Real dispersion σ	k_a (MPa μm$^{1/2}$)	τ_0 (MPa)
Self consistent scheme	0	113.17	22.40
Unimodal	0.02	113.44	20.11
Lognormal ($\sigma = 0.1$)	0.08	111.19	20.31
Lognormal ($\sigma = 0.5$)	0.34	69.81	22.02
Lognormal ($\sigma = 1$)	0.47	46.44	21.72

Table 2
Determination of the slip system reaching first the local plastic criterion for a microstructure of 100 grains with different discretization grids.

Size of grid	Voxels/grain	$p = 0$			$p = 2$		
		Grain r	System k	$\hat{\tau}^r_k$	Grain	System	$\hat{\tau}^r_k$
10	10	77	7	0.4929	80	6	0.5692
20	80	77	7	0.4948	80	6	0.5613
30	270	59	5	0.4958	80	6	0.5646
40	640	59	5	0.4954	80	6	0.5627
50	1250	77	7	0.4954	80	6	0.5609
64	2621	77	7	0.4949	80	6	0.5626
80	5120	59	5	0.4947	80	6	0.5622
100	10,000	59	5	0.4944	80	6	0.5627
144	29,859	59	5	0.4929	80	6	0.5605
160	40,960	59	5	0.4930	80	6	0.5610

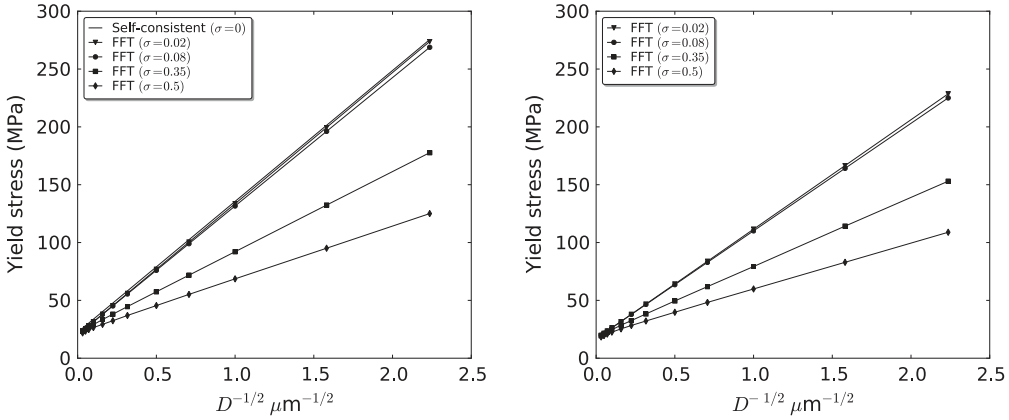

Fig. 15. Effective Hall–Petch relation for log-normal grain size distribution. $p = 0$ (left) and $p = 1$ (right).

dispersion parameters σ. The corresponding yield stress has been evaluated with the proposed yield criterion for two values of the p parameter: $p = 0$ which amounts to neglect the stress fluctuations and $p = 1$. The results are plotted on Fig. 15. For low value of the dispersion parameter ($\sigma = 0.02$) the FFT results almost coincide with the self-consistent estimate. For the criterion based on the intragranular average stress ($p = 0$), a decrease of the effective Hall–Petch slope is described when the dispersion parameter increases (Fig. 15 and Table 3). This full-field result on Laguerre polycrystalline microstructures agrees with previous results obtained with the self-consistent approach [13].

However, as explained above, a yield criterion neglecting the stress fluctuation at the grain scale is likely to provide irrealistic estimates. In this context, it is thus interesting to consider the more general criterion that we have proposed with a non-vanishing value of the p parameter. As shown in Fig. 15 for $p = 1$, our results show that the incorporation of the stress field heterogeneity significantly affects the effective Hall–Petch slope. These observations highlight the combined influence of the grain size distribution and the intragranular stress field fluctuations for the description of the inception of plasticity.

4. Conclusion

A numerical framework encompassing the generation of three-dimensional polycrystalline microstructures and FFT full-field computations has been proposed to study the influence of the grain size distribution on the inception of plasticity. Concerning the generation of artificial microstructures, it has been shown that the combination of dense-sphere packing and Laguerre diagrams provides a convenient way to produce microstructures with a prescribed grain size distribution. Besides, this procedure has been extended to situations of morphological anisotropy representative of extruded or laminated polycrystals. By adopting an explicit grain size dependence of the critical resolved shear stresses and using a local plastic criterion taking into account the intragranular stress field fluctuations, the macroscopic Hall–Petch slope, corresponding to the initial yield surface, has been obtained. A significant influence of the stress heterogeneity is described. Our full-field results also confirm previous results from the literature derived in the framework of mean-field approaches.

Appendix A. Grain size distribution from EBSD images

A.1. Hypothesis and frame

EBSD technics provide data on orientations of grains on the surface. Stereology enables use of this slice so as to recover statistic datas on the polycrystal. Hypothesis must be made on grain shape. Statistic characteristics of grain shape and spatial repartition is expected independent to the frame. Grains are also expected to be almost spherical, with a low aspect ratio. The first hypothesis has a strong effect on pair correlation function, which depends only on distance between points. The second hypothesis enable a simple stereological study of the EBSD image (see Figs. A.1 and A.2).

Three different technics were used. The first one is the one described by Humphreys [43]. The second one is based on an article of Sahagian and Proussevitch [44] and more recent work of Jagnow [45]. The last one is similar to the second one but hypothesis are changed (see Table A.1 and A.2).

Some grains were not considered is this study, namely:

- All the grains that touched the boundary of the image.
- All the grains that were represented by less than 10 pixels.

So as to compare various grain size repartition functions, all sizes were divided by the medium size. The pixel dimension of built microstructure is then chosen so that this medium size is similar. The medium size is such that half of the material is made of grains below this size and half above. Definition of grain size repartition function can be found in [29]. Using the average grain size may be more meaningful from a statistical point of view but medium size corresponds to medium volume which is not the case with averages.

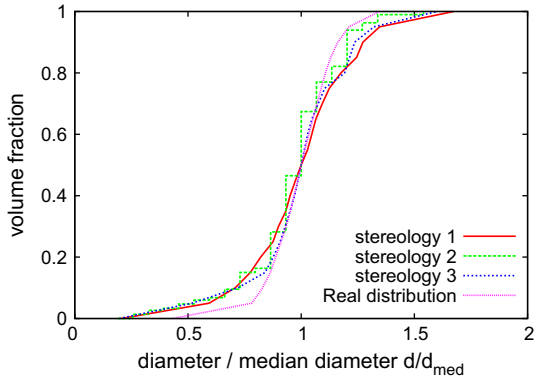

Fig. A.1. Grain equivalent diameter repartition function for the different technics used. Violet: real function from the 3D Voronoi diagram. Red: function from first technic. Green: function from second technic. The steps come from the hypothesis of discrete radius. Blue: function from third technic. (For interpretation of the references to colour in this figure legend, the reader is referred to the web version of this article.)

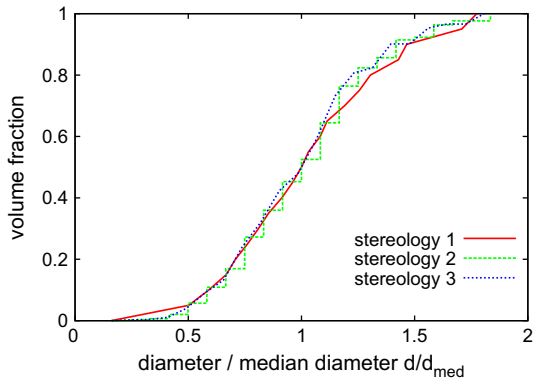

Fig. A.2. Grain equivalent diameter repartition function for the different technics used, zirconium EBSD image. Red: function from first technic. Green: function from second technic. The steps come from the hypothesis of discrete radius. Blue: function from third technic. (For interpretation of the references to colour in this figure legend, the reader is referred to the web version of this article.)

Table A.1
Estimates of medium diameter, Voronoi diagram.

	Medium diameter	Average diameter
Exact	0.1024	0.1017
Using technique 1	0.0601	0.0597
Using technique 2	0.0944	0.0909
Using technique 3	0.0908	0.0901

Table A.2
Estimates of medium diameter, zirconium EBSD image.

	Medium diameter (μm)	Average diameter (μm)
Technic 1	22.64	23.00
Technic 2	31.68	32.15
Technic 3	32.17	31.98

A.2. Stereologic technics

A.2.1. First technic

The first approach is based on an article by Humphreys [43]. The equivalent diameter of a grain is artificially linked to the apparent section of this grain. If D is the equivalent diameter of the grain area, the equivalent diameter of the grain ECD is given by $ECD = 0.816 \times D$.

The volumic ratio of grains of corresponding size is estimated through:

$$\frac{V_G}{V_{total}} = \frac{A_G}{A_{total}}$$

This method is very practical but a direct link between section area and volume is clearly a potential source of mistake. Other technics exist that take account of the probabilistic feature of such link will give better results.

A.2.2. Second technic

The second one is based on an article of Sahagian and Proussevitch [44] and more recent work of Jagnow [45]. This method takes account of the fact that a big grain may be hiden behind a small section.

As the image is supposed to contain all the statistical data on grain size, the bigger section area correspond to the bigger grain. An hypothesis is added on grain size distribution. There are 20 different radius R_i between the bigger one and the smaller one. The radius are placed in arithmetic sequence or geometric sequence. First, the number of sections per area unit N_{Ai} on the image is calculated. N_{Ai} is the number of sections of radius between R_{i-1} et R_i per area unit. Numbers of grains per volume unit N_{Vi} are then estimated. N_{Vi} represents the number of grain of equivalent radius R_i per unit volume. The sections of radius between R_{i-1} and R_i correspond to grains of equivalent radius higher than R_{i-1}, here higher than or equal to R_i. So N_{Ai} is expressed using N_{Vj}, where $j \geqslant i$:

$$N_{Ai} = \sum_{j \geqslant i} H(R_j) P(R_{i-1}, R_i, R_j) N_{Vj}$$

where

- $H(R)$ is the average projected high and worths $2R$ (sphere)
- $P(R_{i-1}, R_i, R)$ is the probability to obtain a section radius between R_{i-1} et R_i by cutting a sphere of radius R. It worths:

$$P(R_{i-1}, R_i, R) = \frac{1}{R}\left(\sqrt{R^2 - R_{i-1}^2} - \sqrt{R^2 - R_i^2}\right)$$

After calculating N_{Vj} by successive substitution, grain size repartition function is calculated. At each radius R_i, the repartition function has a $\frac{4\pi}{3} R_i^3 N_{Vi}$ high step. This method is not very accurate for small radius. The hypothesis or discrete radius may trigger errors. More realistic hypothesis can be adopted as in the third technic.

A.2.3. Third technic

This technic is close to the second one, expect the hypothesis on the grain size distribution function has changed. The third method supposes that the repartition function F is a piecewise linear function. It is affine on each interval $[R_{i-1}, R_i]$.

On $[R_{i-1}, R_i]$

$$\frac{dF}{dR}(R) = \frac{dN_V}{dR}(R) \frac{4\pi}{3} R^3 = \alpha_i$$

It is still true that:

$$N_{Ai} = \int_{R_{i-1}}^{\infty} H(R) P(R_{i-1}, R_i, R) \frac{dN_V}{dR}(R) dR$$

$$\underline{N_A} = \underline{\underline{K}}\,\underline{\alpha}$$

$\underline{\underline{K}}$ is an upper triangular matrix. Its coefficients are:

- $j < i$: $K_{ij} = 0$
- $j = i$: $K_{ij} = \int_{R_{j-1}}^{R_i} \frac{2}{3\pi} \frac{\sqrt{R^2 - R_{i-1}^2}}{R^3} dR$
- $j > i$: $K_{ij} = \int_{R_{j-1}}^{R_j} \frac{2}{3\pi} \frac{\sqrt{R^2 - R_{i-1}^2} - \sqrt{R^2 - R_i^2}}{R^3} dR$

These integrals can be calculated using the primitive of $\frac{\sqrt{x^2-1}}{x^3}$:

$$-\frac{\sqrt{x^2-1}}{2x^2} - \frac{\pi}{4} + \frac{1}{2}\arctan\left(\sqrt{x^2-1}\right)$$

A.3. Comparison of results

The three methods were applied to a fake EBSD image calculated with the help of a Voronoi tessellation. The grain size repartition function can be therefore estimated with both the exact calculated volumes of grains or the EBSD image and stereology technics. 2000 germs were used. The produced section contains 600×600 dots on a hexagonal lattice. 2244 sections were observed on this slice which reproduces many times the periodic square. Medium diameter and average diameter were calculated with the different methods.

Technics that take account of the probability in linking sections and volumes seem more accurate. So as to compare different

scales, the ratio $\frac{\text{diameter}}{\text{median diameter}}$ is plotted. The different technics leave similar results. All of them overestimate the volume ratio of small grains. The first one forgets that little section may come from big grains. Errors in other methods may be triggered by successive determination of numbers of grain in each radius interval starting from the bigger ones. The sphere not being spherical may be another potential source of mistake. At last, the image may not contain all the statistical data on the microstructure.

Those three methods were applied on a real EBSD image of a zirconium polycrystal. The image is $700 \times 430\,\mu m^2$ wide. Mesured points are on an hexagonal lattice of 466×331 points. 1018 grains were seen on the image and only 665 were used for this study.

References

[1] B.L. Adams, T. Olson, Progr. Mater. Sci. 43 (1998) 1–88.
[2] S. Torquato, Random Heterogeneous Materials, Springer, 2002.
[3] E.O. Hall, Proc. Phys. Soc. London B64 (1951) 747–753.
[4] N.J. Petch, J. Iron Steel Inst. 174 (1953) 25–28.
[5] S. Forest, F. Barbe, G. Cailletaud, Int. J. Solids Struct. 37 (2000) 7105–7126.
[6] M.E. Gurtin, J. Mech. Phys. Solids 50 (2002) 5–32.
[7] N. Cordero, S. Forest, E. Busso, S. Berbenni, M. Cherkaoui, Comput. Mat. Sci. 52 (2012) 7–13.
[8] M.F. Ashby, Phil. Mag. 21 (1970) 399–424.
[9] A. Acharya, A.J. Beaudoin, J. Mech. Phys. Solids 48 (2000) 2213–2230.
[10] L.P. Evers, D.M. Parks, W.A.M. Brekelmans, M.G.D. Geers, J. Mech. Phys. Solids 50 (2002) 2403–2424.
[11] G.J. Weng, J. Mech. Phys. Solids 31 (1983) 193–203.
[12] K.J. Kurzydlowski, Scripta Mater. 24 (1990) 879–883.
[13] S. Berbenni, V. Favier, M. Berveiller, Int. J. Plasticity 23 (2007) 114–142.
[14] J.W. Hutchinson, Proc. R. Soc. Lond. A319 (1970) 247–272.
[15] R. Brenner, R.A. Lebensohn, O. Castelnau, Int. J. Solids Struct. 46 (2009) 3018–3026.
[16] H. Moulinec, P. Suquet, Comput. Methods Appl. Mech. Eng. 157 (1998) 69–94.
[17] R.A. Lebensohn, Acta Mater. 49 (2001) 2723–2737.
[18] W. Ludwig, S. Schmidt, E.M. Lauridsenc, H.F. Poulsen, J. Appl. Cryst. 41 (2008) 302–309.
[19] W. Ludwig, A. King, P. Reischig, M. Herbig, E.M. Lauridsen, S. Schmidt, H. Proudhon, S. Forest, P. Cloetens, S.R. du Roscoat, J.Y. Buffière, T.J. Marrow, H.F. Poulsen, Mater. Sci. Eng. A 524 (2009) 69–76.
[20] A. Belkhabbaz, R. Brenner, N. Rupin, B. Bacroix, J. Fonseca, Procedia Eng. 10 (2011) 1883–1888.
[21] A. Musienko, A. Tatschl, K. Schmidegg, O. Kolednik, R. Pippan, G. Cailletaud, Acta Mater. 55 (2007) 4121–4136.
[22] B.D. Lubachevsky, F.H. Stillinger, J. Stat. Phys. 60 (1990) 561–583.
[23] F. Aurenhammer, SIAM J. Comput. 16 (1987) 78–96.
[24] P. Zhang, D. Balint, J. Lin, Phil. Mag. A 91 (2011) 4555–4573.
[25] S. Kumar, S.K. Kurtz, Acta Metall. Mater. 42 (1994) 3917–3927.
[26] S. Kumar, S.K. Kurtz, V.K. Agarwala, Acta Mechanica 114 (1996) 203–216.
[27] M. Nygards, P. Gudmundson, Comput. Mater. Sci. 24 (2002) 513–519.
[28] A. Zeghadi, F. N'Guyen, S. Forest, A.-F. Gourgues, O. Bouaziz, Phil. Mag. A 87 (2007) 1401–1424.
[29] A. Lachihab, Un modèle numérique pour les composites biphasés matrice-inclusions rigides: application à la détermination des propriétés élastiques et en fatigue des enrobés bitumineux, Ph.D. thesis, Ecole Nationale des Ponts et Chaussées, France, 2004.
[30] F. Aurenhammer, H. Imai, Geometriae Dedicata 27 (1988) 65–75.
[31] M. Zemek, Regular Triangulation in 3D and its applications, Technical Report, University of West Bohemia, 2009.
[32] A. Donev, S. Torquato, F.H. Stillinger, J. Comput. Phys. 202 (2005) 737–764.
[33] E. Ghossein, M. Lévesque, Int. J. Solids Struct. 49 (2012) 1387–1398.
[34] Z. Fan, Y. Wu, X. Zhao, Y. Lu, Comput. Mater. Sci. 29 (2004) 301–308.
[35] A. Benabbou, H. Borouchaki, P. Laug, J. Lu, Int. J. Numer. Meth. Eng. 80 (2009) 425–454.
[36] R. Jafari, M. Kazeminezhad, Comput. Mater. Sci. 50 (2011) 2698–2705.
[37] K. Hitti, P. Laure, T. Coupez, L. Silva, M. Bernacki, Comput. Mater. Sci. 61 (2012) 224–238.
[38] T. Kanit, S. Forest, I. Galliet, V. Mounoury, D. Jeulin, Int. J. Solids Struct. 40 (2003) 3647–3679.
[39] F.E. Houdaigui, S. Forest, A.-F. Gourgues, D. Jeulin, in: Y. Bai, (Ed.), IUTAM Symposium on Mechanical Behavior and Micro-Mechanics of Nanostructured Materials, 2007, pp. 171–180.
[40] A.V. Hershey, J. Appl. Mech. 21 (1954) 236–240.
[41] E. Kröner, Z. Physik 151 (1958) 504–518.
[42] R. Brenner, O. Castelnau, L. Badea, Proc. R. Soc. Lond. A460 (2004) 3589–3612.
[43] P.J. Humphreys, J. Mater. Sci. 36 (2001) 3833–3854.
[44] D.L. Sahagian, A.A. Proussevitch, J. Volcanology Geothermal Res. 84 (1998) 173–196.
[45] R.C. Jagnow, Stereological Techniques for Synthesizing Solid Textures from Images of Aggregate Materials, Ph.D. thesis, Massachusetts Institute of Technology, 2004.